Generalized contrast-to-noise ratio as a metric of photoacoustic image quality

Kempski, Kelley, Graham, Michelle, Wiacek, Alycen, Gubbi, Mardava, Lediju Bell, Muyinatu

Kelley M. Kempski, Michelle Graham, Alycen Wiacek, Mardava Gubbi, Muyinatu A. Lediju Bell, "Generalized contrast-to-noise ratio as a metric of photoacoustic image quality," Proc. SPIE 11642, Photons Plus Ultrasound: Imaging and Sensing 2021, 116421C (5 March 2021); doi: 10.1117/12.2579055

Event: SPIE BiOS, 2021, Online Only

Generalized Contrast-to-Noise Ratio as a Metric of Photoacoustic Image Quality

Kelley M. Kempski[a], Michelle Graham[b], Alycen Wiacek[b], Mardava Gubbi[b], and Muyinatu A. Lediju Bell[b,c]

[a]Department of Biomedical Engineering, Johns Hopkins University, Baltimore, MD
[b]Department of Electrical & Computer Engineering, Johns Hopkins University, Baltimore, MD
[c]Department of Computer Science, Johns Hopkins University, Baltimore, MD

ABSTRACT

Multiple image quality metrics are currently available to assess target detectability in photoacoustic images. Common metrics include contrast, contrast-to-noise ratio (CNR), and signal-to-noise ratio (SNR). The generalized contrast-to-noise ratio (gCNR) is a relatively new image quality metric to assess the probability of photoacoustic target detectability. This paper demonstrates the applicability of gCNR to assess photoacoustic image quality using simulated and experimental images created with delay-and-sum (DAS), short-lag spatial coherence (SLSC), generalized coherence factor weighting combined with DAS (GCF+DAS), and minimum variance (MV) beamforming. Images were created from data acquired with a fixed light source with output energy values increasing from 2 mJ to 35 mJ. The gCNR converged to 0.93, 0.98, 0.99, and 0.85 for DAS, SLSC, GCF+DAS, and MV beamforming, respectively, at energies of approximately 20, 10, 10, and 20 mJ, respectively. These results indicate that gCNR has the potential to determine the minimum laser energy needed to maximize the detectability of a photoacoustic target for any given image formation method.

1. INTRODUCTION

Photoacoustic imaging is performed by irradiating optical absorbers with a light source, which causes thermal expansion and subsequent emission of an acoustic pressure wave that is received by an ultrasound transducer.[1,2] The feasibility of photoacoustic imaging has been demonstrated for a variety of future surgical guidance applications,[3] including tumor therapy guidance,[4–6] biopsy,[7,8] liver surgeries,[9] cardiac catheter-based interventions,[10] and robotic surgeries.[11] The quality of these photoacoustic images has traditionally been assessed using contrast, contrast-to-noise ratio (CNR), and signal-to-noise ratio (SNR). However, in a practical setting, if a photoacoustic target is perfectly distinguishable from its background, there is no clinical benefit to devising new beamformers and image processing methods to increase contrast, CNR, and SNR. In addition, these traditional image quality metrics suffer from limitations that include the lack of an upper bound, magnitudes that are not intuitive, and difficulty determining the detectability of a target based solely on quantitative metrics (e.g., in text-only abstracts).[12,13]

The generalized contrast-to-noise ratio (gCNR) was recently developed to overcome these limitations,[12] and its applicability to photoacoustic imaging was subsequently investigated.[13] Introduced as a probabilistic measurement of the separability of a target relative to a background, gCNR is defined as:

$$\text{gCNR} = 1 - \sum_{k=0}^{N-1} \max\{h_i(x_k), h_o(x_k)\}. \tag{1}$$

where h_i and h_o represent the histograms for the regions inside and outside the target, respectively, N is the number of bins, and k is the index of the bin.

This paper expands our initial investigations of the utility of gCNR for photoacoustic images[13] by demonstrating its applicability to assess the quality of additional beamformers and to assess maximum laser energy requirements for each beamformer to achieve the maximum possible gCNR value of 1.

Photons Plus Ultrasound: Imaging and Sensing 2021, edited by Alexander A. Oraevsky
Lihong V. Wang, Proc. of SPIE Vol. 11642, 116421C · © 2021 SPIE
CCC code: 1605-7422/21/$21 · doi: 10.1117/12.2579055

2. METHODS

2.1 Data Acquisition

Simulated photoacoustic channel data were generated using the k-Wave toolbox.[14] A linear transducer was defined with 0.3 mm pitch, 0.06 mm kerf, and 128 elements. The transducer had a center frequency of 5 MHz and 2-8 MHz bandwidth. A 6 mm-diameter circular target containing randomly distributed optical absorbers with a spatial density of 299 absorbers/mm^2 was placed at the center of a 23.1 mm $\times$ 38.4 mm phantom. Fifteen simulated images with 0 dB channel SNR were generated.

Experimental photoacoustic data were acquired with an Alpinion L3-8 linear transducer connected to an Alpinion ECUBE 12R ultrasound system (Alpinion, Seoul, Korea) and synchronized with a Phocus Mobile laser (OPOTEK, Carlsbad, CA) connected to a 5 mm-diameter fiber bundle. The laser emitted 750 nm light. The 5 mm-diameter fiber bundle was placed in a plastic tub filled with water, and the ultrasound probe was positioned to image the circular cross-section of the fiber bundle tip. Output energies from the fiber bundle tip ranged 2-35 mJ, and 15 frames of photoacoustic channel data were acquired for each energy level.

2.2 Data Analysis

Photoacoustic channel data were delayed to account for time arrival differences and subsequently beamformed with four beamforming techniques, specifically delay-and-sum (DAS), short-lag spatial coherence (SLSC),[6,15,16] generalized coherence factor weighting applied to DAS (GCF+DAS),[17] and minimum variance (MV)[18] beamforming. DAS beamforming sums the delayed signals to directly display signal amplitude. SLSC beamforming computes the spatial coherence of the delayed signals as a function of element spacing (i.e., spatial lag) and sums these coherence functions up to a specific short-lag value, M, to directly display signal coherence. GCF weighting applies pixel-by-pixel multiplication of the DAS image with factors representing the focusing quality of each pixel in the DAS image. MV beamforming iteratively determines optimal weights for each channel prior to summation.[18]

2.3 Image Quality Assessment

Contrast and gCNR were calculated for each DAS, SLSC, GCF+DAS, and MV beamformed image after normalization and prior to log compression. Contrast was calculated using the equation:

$$\text{Contrast} = 20\log_{10}\left(\frac{\mu_i}{\mu_o}\right) \tag{2}$$

where μ_i and μ_o represent the mean pixel amplitude within regions of interest (ROIs) inside and outside the target, respectively. The gCNR was calculated using Eq. 1 with $N = 256$ bins. The ROIs for the simulated data were 6 mm-diameter circles, with the background ROI offset +15 mm laterally from the target ROI. The ROIs for the experimental data were 4 mm-diameter circles, with the background ROI offset -7.5 mm laterally from the target ROI.

3. RESULTS

Fig. 1 shows example simulated (top) and experimental (bottom) beamformed images using DAS, SLSC, GCF+DAS, and MV beamformers. The DAS and GCF+DAS images are qualitatively similar, containing a mixture of bright and dark pixel regions within the target for both simulated and experimental datasets. However, the DAS image has greater background noise compared to the GCF+DAS image. The SLSC images have the least dark regions within the target. The MV images have the least clearly defined target boundaries.

Fig. 2 shows the mean gCNR and contrast ± one standard deviation of DAS, SLSC, GCF+DAS, and MV beamformed experimental images as a function of energy. Results from images simulated with 0 dB channel SNR are shown as the independent data points in these plots. The SLSC and GCF+DAS beamformers produced images with nearly perfectly detectable targets (i.e., gCNR ≥ 0.98). The gCNR values converge after a specific laser energy level (e.g., 10 mJ for SLSC and GCF+DAS, 20 mJ for DAS and MV), indicating that additional increases in laser energy do not provide increased target detectability. The corresponding contrast measurements for these beamformers are unhelpful with regard to making a definitive determination on this detail, producing values ranging 11.2-39.4 dB.

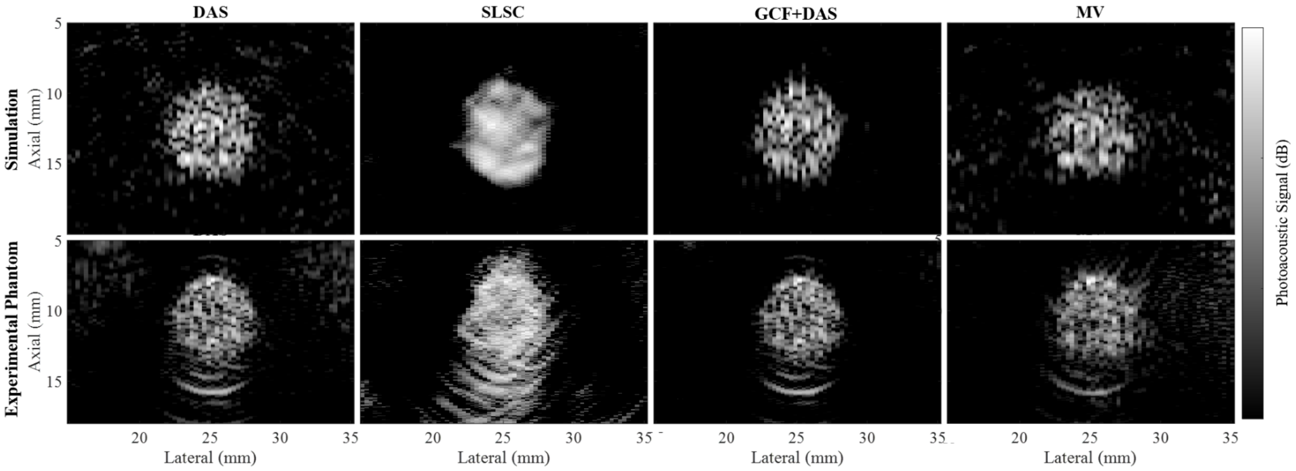

Figure 1. Example simulated (top) and experimental (bottom) DAS, SLSC (M = 5), GCF+DAS, and MV beamformed images.

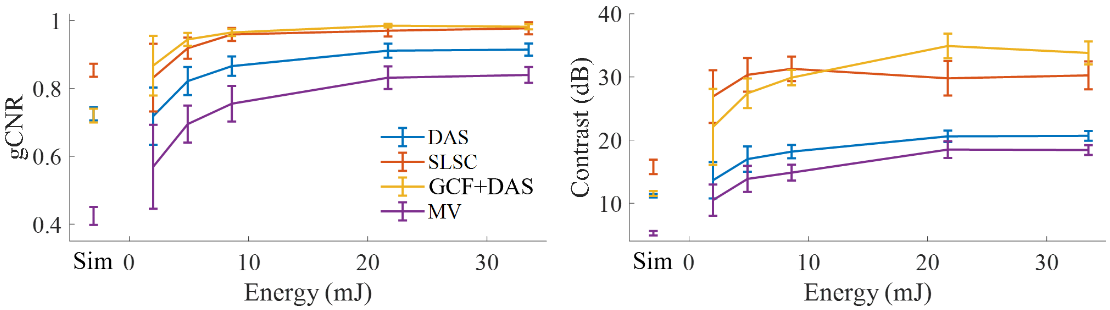

Figure 2. Mean gCNR and contrast ± one standard deviation as a function of laser energy for DAS, SLSC (M = 5), GCF+DAS, and MV beamformed experimental images. The independent data point represents gCNR and contrast measurements from simulated images generated with 0 dB channel SNR.

4. DISCUSSION

This paper presents two key benefits to using gCNR as a metric of photoacoustic image quality. First, the bounded gCNR metric (which only produces values $\in [0, 1]$) is a more intuitive prediction of target detectability than contrast measurements, which can produce large values with no useful increase in image quality. For example, this advantage of gCNR over traditional image quality metrics was observed with the SLSC and GCF+DAS beamformers (Fig. 2), where a large variation in contrast of up to 28.2 dB was observed across targets with near perfect detectability (i.e., when gCNR was ≥ 0.98).

The second benefit is that gCNR has the potential to define beamformer-specific maximum laser energy requirements. Appropriate selection of laser energies is critical for avoiding laser-induced tissue damage. As demonstrated in Fig. 2, gCNR asymptotes to a maximum value as energy increases, indicating that additional laser energy increases beyond a specific value provides diminishing gains in image quality. Therefore, calculating gCNR has the potential to serve as an objective metric to mitigate patient exposure to unnecessarily high laser energies that do not provide additional increases in photoacoustic target detectability. Overall, these results are promising for the possible incorporation of gCNR as a reported parameter to assist with assessing the safety of a particular imaging system configuration.

5. CONCLUSION

The work presented in this paper is the first to demonstrate the feasibility of using gCNR for selecting experimental laser energies to maximize image quality and minimize the risk of laser damage. The applicability of gCNR as a photoacoustic image quality metric is demonstrated with simulated and experimental datasets with four beamformers. In addition to providing an intuitive, probabilistic measurement of target detectability and information for laser energy selections, gCNR is robust to multiple limitations of traditional image quality metrics.

Acknowledgments

Funding was provided by National Science Foundation (NSF) CAREER Award ECCS-1751522, NSF SCH Award NSF IIS-2014088, and in part by NSF Graduate Research Fellowship DGE1746891.

REFERENCES

1. R. Bouchard, O. Sahin, and S. Emelianov, "Ultrasound-guided photoacoustic imaging: Current state and future development," *IEEE Transactions on Ultrasonics, Ferroelectrics, and Frequency Control* , 2014.
2. M. Xu and L. V. Wang, "Photoacoustic imaging in biomedicine," *Review of Scientific Instruments* **77**(041101), pp. 1–22, 2006.
3. M. A. Lediju Bell, "Photoacoustic imaging for surgical guidance: Principles, applications, and outlook," *Journal of Applied Physics* **128**(6), p. 060904, 2020.
4. J. L. Su, R. R. Bouchard, A. B. Karpiouk, J. D. Hazle, and S. Y. Emelianov, "Photoacoustic imaging of prostate brachytherapy seeds," *Biomed. Opt. Express* **2**, pp. 2243–2254, Aug 2011.
5. T. Harrison and R. J. Zemp, "Coregistered photoacoustic-ultrasound imaging applied to brachytherapy.," *Journal of Biomedical Optics* **16**, p. 080502, Aug 2011.
6. M. A. Lediju Bell, N. Kuo, D. Y. Song, and E. M. Boctor, "Short-lag Spatial Coherence Beamforming of Photoacoustic Images for Enhanced Visualization of Prostate Brachytherapy Seeds.," *Biomedical Optics Express* **4**(10), pp. 1964–77, 2013.
7. C. Kim, T. N. Erpelding, L. Jankovic, and L. V. Wang, "Performance benchmarks of an array-based hand-held photoacoustic probe adapted from a clinical ultrasound system for non-invasive sentinel lymph node imaging.," *Philosophical transactions. Series A, Mathematical, physical, and engineering sciences* **369**, pp. 4644–50, Nov 2011.
8. D. Piras, C. Grijsen, P. Schutte, W. Steenbergen, and S. Manohar, "Photoacoustic needle: minimally invasive guidance to biopsy," *Journal of Biomedical Optics* **18**(7), p. 070502, 2013.
9. K. M. Kempski, A. Wiacek, M. Graham, E. González, B. Goodson, D. Allman, J. Palmer, H. Hou, S. Beck, J. He, and M. A. L. Bell, "In vivo photoacoustic imaging of major blood vessels in the pancreas and liver during surgery," *Journal of Biomedical Optics* **24**(12), p. 1, 2019.
10. M. Graham, F. Assis, D. Allman, A. Wiacek, E. Gonzalez, M. Gubbi, J. Dong, H. Hou, S. Beck, J. Chrispin, and M. A. L. Bell **39**(4), pp. 1015–1029, 2020.
11. N. Gandhi, M. Allard, S. Kim, P. Kazanzides, and M. Lediju Bell, "Photoacoustic-based approach to surgical guidance performed with and without a da vinci robot," *Journal of Biomedical Optics* **22**, p. 1, 08 2017.
12. A. Rodriguez-Molares, O. M. H. Rindal, J. D'hooge, S.-E. Måsøy, A. Austeng, M. A. L. Bell, and H. Torp, "The generalized contrast-to-noise ratio: a formal definition for lesion detectability," *IEEE Transactions on Ultrasonics, Ferroelectrics, and Frequency Control* **67**(4), pp. 745–759, 2020.
13. K. M. Kempski, M. T. Graham, M. R. Gubbi, T. Palmer, and M. A. L. Bell, "Application of the generalized contrast-to-noise ratio to assess photoacoustic image quality," *Biomedical Optics Express* **11**(7), pp. 3684–3698, 2020.
14. B. E. Treeby and B. T. Cox, "k-wave: Matlab toolbox for the simulation and reconstruction of photoacoustic wave fields," *Journal of Biomedical Optics* **15**(2), p. 021314, 2010.
15. M. A. Lediju, G. E. Trahey, B. C. Byram, and J. J. Dahl, "Short-lag spatial coherence of backscattered echoes: imaging characteristics," *IEEE Transactions on Ultrasonics, Ferroelectrics and Frequency Control* **58**, pp. 1377–1388, Jul 2011.
16. M. T. Graham and M. A. L. Bell, "Photoacoustic spatial coherence theory and applications to coherence-based image contrast and resolution," *IEEE Transactions on Ultrasonics, Ferroelectrics, and Frequency Control* **67**(10), pp. 2069–2084, 2020.
17. P.-C. Li and M.-L. Li, "Adaptive imaging using the generalized coherence factor," *IEEE transactions on ultrasonics, ferroelectrics, and frequency control* **50**(2), pp. 128–141, 2003.

18. J. F. Synnevag, A. Austeng, and S. Holm, “Adaptive beamforming applied to medical ultrasound imaging,” *IEEE transactions on ultrasonics, ferroelectrics, and frequency control* **54**(8), pp. 1606–1613, 2007.